Efficient Self-Attention Based Joint Optimization for Lithology and Petrophysical Parameter Estimation in the Athabasca Oil Sands

M Quamer Nasim[a], Dr. Paresh Nath Singha Roy[a,b], Dr. Adway Mitra[c]*

[a*]M Quamer Nasim (Corresponding Author) - Department of Geology and Geophysics, Indian Institute of Technology, Kharagpur, 721302, West Bengal, India; quamer.nasim@kgpian.iitkgp.ac.in; quamer23nasim38@gmail.com

[a]Dr. Paresh Nath Singha Roy - Department of Geology and Geophysics, Indian Institute of Technology, Kharagpur, 721302, West Bengal, India; pareshsr@gg.iitkgp.ac.in

[b]Dr. Paresh Nath Singha Roy - Deysarkar Centre of Excellence in Petroleum Engineering, Indian Institute of Technology, Kharagpur, 721302, West Bengal, India; pareshsr@gg.iitkgp.ac.in

[c]Dr. Adway Mitra - Centre of Excellence in Artificial Intelligence, Indian Institute of Technology, Kharagpur, 721302, West Bengal, India**;** adway@cai.iitkgp.ac.in

Key words - Lithology Identification, Petrophysical Parameter Estimation, Multitask Learning, Self-Attention, Auto-Regressive Vision Transformer, Low Rank Adaptation

This manuscript is a post-print submitted to EarthArXiv. This is the pre-publsihed version of the manuscript. Published version of this manuscript in available in the Journal of Applied Geophysics under DOI: https://doi.org/10.1016/j.jappgeo.2024.105532.

Abstract

Accurately identifying lithology and petrophysical parameters, such as porosity and water saturation, are essential in reservoir characterization. Manual interpretation of well-log data, the conventional approach, is not only labor-intensive but also susceptible to human errors. To address these challenges of lithology identification and petrophysical parameter estimation in the Athabasca Oil Sands area, this study introduces an AutoRegressive Vision Transformer (ARViT) model for lithology and petrophysical parameter prediction. The effectiveness of ARViT lies in its self-attention mechanism and its ability to handle data sequentially, allowing the model to capture important spatial dependencies within the well-log data. This mechanism enables the model to identify subtle spatial and temporal relationships among various geophysical measurements. The model is also interpretable and can serve as an assistive tool for geoscientists, enabling faster interpretation while reducing human bias. The interpretable nature of the model should assist geoscientists in conducting faster quality checks of the predictions, ensuring that errors are not propagated to subsequent stages. This study adopts a multitask learning approach, jointly optimising the model's performance across multiple tasks simultaneously. To evaluate the effectiveness of the ARViT model, we conducted series of experiments and comparisions, testing it against traditional artificial neural networks (ANN), Long Short-Term Memory (LSTM), and Vision Transformer (ViT) models. To showcase the versatility of ARViT, we apply Low-Rank Adaptation (LoRA) to a different smaller dataset, showing its potential to adapt to different geological contexts. LoRA not only helps in model adaptability but also helps to reduce the number of trainable parameters. Our findings demonstrate that ARViT outperforms ANN, LSTM, and ViT in estimating lithological and petrophysical parameters. While lithology prediction has been a well-explored field, ARViT's unique blend of features, including its

self-attention mechanism, autoregression, and multitask approach along with efficient fine tuning using LoRA, sets it apart as a valuable tool for the complex task of lithology prediction and petrophysical parameter estimation.

Key words - Lithology Identification, Petrophysical Parameter Estimation, Multitask Learning, Self-Attention, Auto-Regressive Vision Transformer, Low Rank Adaptation

1. Introduction

The accurate characterization of lithology and its petrophysical parameter estimation are cornerstones in hydrocarbon exploration, playing a crucial role in understanding subsurface formations, resource estimation, and reservoir management within the oil and gas industry (Mohamed et al., 2019). Primarily, Geoscientists rely on cores extracted while drilling to identify lithology from subsurface formations. There are other indirect methodologies using which geoscientist identify lithologies, including parameters from drilling operationssuch as rate of penetration, weight on bit, as well as well-logging data like gamma-ray (GR), bulk density, neutron porosity (NPHI), density porosity (DPHI), and resistivity logs (Serra, 1986, 1964). However, indirect methods have their own uncertainties, and interpretations of parameters can vary depending on the skillset of interpreters. Manual interpretation is time-consuming and susceptible to human bais.

In recent years, geosciences have witnessed significant advancements in AI technology, notably in automating tasks such as velocity inversion (Yang and Ma, 2019), lithology prediction (Meshalkin et al., 2020), seismic facies analysis (Nasim et al., 2022), raster log digitization (Nasim et al., 2024a, 2023), denoising (F. Wang et al., 2022) etc. Several researchers have used machine learning (ML) to map the well logs and drilling parameters to the lithology types to address these issues (Kumar et al., 2022; Zhekenov et al., 2021). Researchers in the past have used classical ML approaches, including Random Forest (RF) (Xie et al., 2018), Decision Tree (DT), Extreme Gradient Boosting (XGBoost) (Sun et al., 2021), etc., to predict lithology and its petrophysical parameters. With the rise in deep learning (DL) techniques, people have also used Artificial Neural Network (ANN), Convolutional Neural Network (CNN) (Alzubaidi et al., 2021), and Recurrent Neural

Network (RNN) (Jiang et al., 2021) to identify lithology and its petrophysical parameter estimation.

In a series of recent studies, researchers have employed various ML and DL techniques to enhance lithology prediction and petrophysical parameter estimations. Kumar et al., 2022 used models such as Support Vector Machine (SVM) (Burges, 1998), DT, RF, ANN, and XGBoost for lithological classification in India's Talcher coalfield, achieving an accuracy of over 88%. Similarly, Mishra et al., 2022 enhanced lithology prediction and reservoir characterization using techniques including K-means clustering (Sinaga and Yang, 2020), K-Nearest Neighbours (KNN) (Cunningham and Delany, 2021), SVM, Principal Component Analysis (PCA) (Wold et al., 1987), and regression. Khalifa et al., 2023 developed an ML model for real-time lithology prediction utilizing drilling data, incorporating models such as RF, Gradient Boost, Linear SVM, AdaBoost, and KNN. This model achieved 95% accuracy and was integrated with a web app for improved real-time geosteering. Ahmadi and Chen, 2019 developed an accurate predictive model for estimating permeability and porosity in oil reservoirs using hybrid ML methods like ANN, genetic algorithms, and fuzzy decision trees, based on petrophysical logs from the Persian Gulf, achieving less than 1% deviation from actual data. Further advances were made by Zhang et al., 2021, who developed a DL method for predicting reservoir porosity using Gated Recurrent Unit (GRU) neural networks (Cho et al., 2014), demonstrating superior accuracy and robustness compared to traditional ML models by effectively analyzing the non-linear relationships between logging data and porosity parameters. Mustafa et al., 2023 employed ANN, adaptive neuro-fuzzy inference system (ANFIS) (Jang, 1993), and functional network (FN) (Zhou et al., 2019) to accurately predict NMR porosity in carbonate reservoirs, demonstrating high accuracy and reliability across diverse datasets from Middle Eastern oil fields. Aditionally, for the task of water saturation estimation, Miah et al., 2020 develop a log data-driven model using ML techniques

such as ANN and SVM for water saturation prediction in reservoirs, showcasing the models' capability to effectively handle non-linear and complex relationships among field data. Hadavimoghaddam et al., 2021 enhanced water saturation prediction from well logs using ML, employing boosting techniques and the Super Learner algorithm without resistivity data, achieving high accuracy. Ibrahim et al., 2022 optimized water saturation prediction in tight gas sandstone using ANN and ANFIS models on well log data, achieving high correlations and low error rates.

In the above mentioned literature survey, we saw separate models for different tasks, such as a different model for lithology prediction and a completely different model for porosity (ϕ) and water saturation (S_w) prediction (Sang et al., 2023; Zhang et al., 2019). Although having separate models is effective, integrating these tasks into a single model could offer substantial benefits. Since all these tasks are interrelated, a single model with multi-tasking capabilities would optimize itself based on the shared knowledge among the different tasks of lithology prediction and petrophysical parameters estimation. This integrated approach would not only enhance performance by utilizing interrelations among the tasks but also significantly reduce the computational costs associated with running three separate models. In this research, we will take advantage of the transformers model (Vaswani et al., 2017) to jointly optimize across multiple tasks, such as lithology prediction, ϕ, and S_w estimation. Transformers models have been revolutionizing AI models in every field. One such transformer model is the Vision Transformer (ViT) (Dosovitskiy et al., 2021), which works well on images. Another type of transformer we will introduce in this research is AutoRegressive ViT (ARViT), which will work in a similar way to LSTM, looking at data sequentially.

ViT represents a groundbreaking paradigm in computer vision (Dosovitskiy et al., 2021). Departing from convolutional architectures, ViTs rely on self-attention mechanisms

(Vaswani et al., 2017) to process image patches individually, enabling global context understanding (Dosovitskiy et al., 2021). By transforming images into sequences, ViTs allow fine-grained interactions between pixels. . The efficacy of ViT in capturing diverse temporal relationships within the data positions it favorably for the utilization and processing of well log in petrophysical properties estimation. Each lithology type and petrophysical parameter is characterized by unique patterns and values in well logs. The self-attention mechanism in ViT facilitate the detection and identification of these well log patterns by dynamically adjusting the importance of different segments within the well log (Kumar, 2021; Sun et al., 2024; J. Wang et al., 2022).

In this research, we introduce ARViT, which extends the ViT model by introducing sequential dependencies in output. By generating each token in a progressive manner, ARViT captures important pixel relationships. With the fusion of autoregressive principles and ViT model, ARViT provides a useful tool for tasks demanding local coherence and holistic understanding. Sequential processing of auto-regression combined with the ViT model helps in enhancing the lithology and petrophysical parameter estimation by sequentially using prior outputs (Lithology, ϕ and S_w) as context, ensuring each depth's analysis builds on the previous depth estimation for improved accuracy and consistency (Nasim et al., 2024b).

In Geoscience, data distribution often changes as we move from one field or one basin to another, necessitating the use of transfer learning to adapt these changes effectively (Nasim et al., 2022). Typically, transfer learning requires full fine-tuning of existing models, which involves significant computational resources, often requiring extensive GPU usage as per the orginal model and thus increasing overall computational and operational costs. To address this challenge, the Low-Rank Adaptation (LoRA) technique has been introduced for the first time in geophysical data. LoRA is a technique that enhances model generalization while

doing transfer learning by reducing the complexity of learned patterns (Hu et al., 2022). Constraining model parameters to a lower-rank representation effectively captures essential well log features while mitigating overfitting. This method finds utility in scenarios with limited data availability, offering improved performance and scalability. It also decreases the computational power required to finetune a large model on a different dataset. Through efficient parameterization, LoRA strikes a balance between model complexity and predictive accuracy. This makes LoRA a valuable technique in geoscience by adapting knowledge of one field or basin onto another, offering a cost-effective and resource-efficient method for applying transfer learning.

In this study, we utilize well-logging data to tackle a multi-faceted challenge encompassing the prediction of lithology, ϕ, and S_w. To address this task, we use the self-attention mechanism combined with auto-regression through the utilization of the ARViT. To assess the effectiveness of our proposed methodology, we undertake a comparative analysis involving three distinct DL architectures: ANN, LSTM, and ViT. Moreover, to enhance model adaptability and facilitate cost-effective transfer learning across domains, we introduce the concept of LoRA into our model. LoRA not only efficiently enables knowledge transfer and adaptation of pre-trained ARViT models to new data domains but also reduces the computational burdens typically associated with such adaptations. This integration improves the versatility of the proposed models, making them more cost-effective for broader applications. We hope that this model can serve as an assistive tool for geoscientists, streamlining the interpretation process and enhancing their objectivity in decision-making, while also helping to reduce human error and biases.

2. Dataset

In this section, we delve into the dataset utilized in our study, encompassing crucial aspects such as the study area, its geological context, and formation characteristics. We also offer insights into the Exploratory Data Analysis (EDA) performed to analyze the dataset's features, Quality Control (QC) measures taken to verify data reliability, and data pre-processing techniques used to enhance input variables for modeling purposes. We will also address the approach employed to divide the dataset into several subsets, allowing for the fair evaluation of model performance and generalization capabilities. Through this comprehensive exploration, we aim to provide a thorough understanding of the dataset's composition and preparation for subsequent analyses and modeling tasks.

2.1.Data Used and Study Area

In this research, we used the well data from the Athabasca Oil Sands Area. The dataset was acquired from the Athabasca Oil Sands Area in the year 1986 through the efforts of the Alberta Geological Survey (Hein et al., 2000; Wynne et al., 1995). The focus of data collection was on the McMurry Formation and the overlying Wabiskaw Member of the Clearwater Formation. The total number of wells available in the Athabasca Oil Sands dataset is about 1012. Fig. 1 illustrates the study area, with the locations of these wells indicated by circles. The geological and stratigraphical settings of the Athabasca Oil Sands area, particularly focusing on the McMurray Formation, illustrate a complex depositional environment (Flach, 1984; Mossop, 1980; Ranger and Pemberton, 1997; Wightman et al., 1995). The region is characterized by pre-Cretaceous unconformity that underlies the Lower Cretaceous units. This unconformity is a key geological boundary that reflects substantial erosional processes and is a significant marker in understanding the regional stratigraphy. The unconformity surface is incised, reflecting the effects of regional erosion, with features

such as paleovalleys, karst landscapes, and structural collapses due to the dissolution of the Elk Point Group evaporites. These erosional features are seen in areas such as the Grosmont High and the Prairie Salt Scarp, which also influence depositional patterns within the overlying formations. The McMurray Formation, the primary focus within the Athabasca Oil Sands unconformably overlies Devonian carbonates of the Beaverhill Lake and Woodbend groups. It is divided into two informal members: the Lower and Upper McMurray. The Lower McMurray is predominantly fluvial, deposited in paleovalleys carved into the karstic pre-Cretaceous landscape. These channels host significant bitumen reservoirs with associated water sands. Compositionally, the Lower McMurray features braided channel-and-bar sands and intraclast mudstone breccias, where the presence of minerals like siderite and pyrite cement can influence resistivity values. Additionally, heavy minerals such as garnet and kyanite are present in the sand units, adding complexity to the reservoir characterization. Above this, the Upper McMurray records an estuarine to nearshore environment, characterized by estuarine channel complexes that often overlie the fluvial sands of the Lower McMurray. It contains bitumen-rich sands, with localized water sands in its lower portion and isolated gas reservoirs in the upper parts. It also shows significant heterogeneity due to multiple cycles of deposition and erosion, marked by estuarine sedimentation and tidal influences. Coastal plain sediments, although largely eroded, occasionally cap the succession, providing evidence of low-gradient drainage patterns influenced by tidal cycles. This upper member is also influenced by the Prairie Salt Scarp, which affects the depositional patterns due to the structural collapse associated with salt dissolution. Each unit within these formations is not only distinct in its depositional environment but also in its mineralogical composition. In the Lower McMurray, autochthonous coal seams interbedded with lacustrine silty clays also indicate an additional lacustrine depositional environment that can locally affect reservoir properties. Minerals such as pyrite and siderite, commonly found along the

basal unconformity and within the McMurray Formation, can significantly decrease the resistivity values. This region's stratigraphic complexity is further complicated by internal disconformities and the variable preservation of the McMurray Formation, influenced by the erosional unconformity at its base and top. Similarly, the Wabiskaw Member of the Clearwater Formation marks the transition from nearshore to fully marine conditions, containing glauconitic sandstones and mudstones that are heavily bioturbated, with distinct marine trace fossils such as Teichichnus and Thalassinoides. This member exhibits marine flooding surfaces and glauconite horizons, indicating periods of transgression and regional marine influence. Understanding these geological settings is crucial for effective exploration and exploitation of the oil sands, providing a framework for the geological model of the area and influencing extraction strategies.

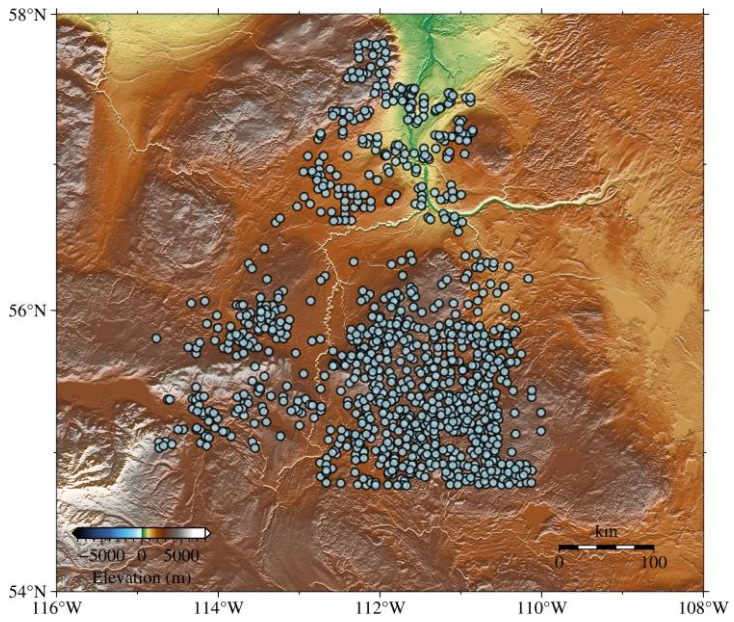

Figure 1 – Study area of the region. Gray blobs shows the wells selected for this study.

The dataset under investigation comprises six distinct lithological categories, namely Sand, Shaly Sand, Cemented Sand, Sandy Shale, Shale, and Coal. From an array of logs available in this dataset, which includes the caliper log (CALI), sonic log (DT), Bulk Density (RHOB), Spontaneous Potential (SP), GR, NPHI, DPHI, Medium Resistivity (ILM), and Deep

Resistivity (ILD), we noted significant data availability issues. Most of the logs, specifically the CALI, DT, ILM, RHOB, and SP, were missing in more than 95% of the wells. Consequently, we selected GR, NPHI, DPHI, and Deep Resistivity (ILD) for our analysis as an independent variable. These logs were consistently available across the dataset and are basic logs that are almost always available in all the wells. Additionally, they contribute significantly to predicting the lithology and estimating petrophysical parameters, making them the most suitable choices for our study. According to the attached report from the Alberta Geological Survey in 1994, core data analysis was conducted on the wells to identify lithologies. Subsequently, the interpreted lithology was populated with petrophysical parameters using various petrophysical equations. However, the core data was not released (Hein et al., 2000; Wynne et al., 1995).

2.2.EDA and Pre-Processing Steps

EDA is crucial in ML, providing insights for lithology identification and petrophysical property estimation. Given the complexity of our problem, we conducted a thorough EDA, utilizing various visualization techniques to understand underlying data patterns, variability, and relationships between independent and dependent variable. Firstly, we have plotted distribution plots and boxplots for different types of logs across each lithology (Fig. 2, 3, and 4). These plots provide valuable insights into the distributional characteristics of each log type within different lithologies, allowing us to discern any notable patterns or discrepencies in the log data. Additionally, these plots serve as a QC step, enabling us to validate whether the provided data aligns with the geological understanding and expectations of each lithology. Abnormal values within well log curves, often caused by tool malfunctions or geological factors, can significantly detoriate model performance if not addressed during the EDA, QC, and data preparation stages. Identifying these abnormalities through EDA and QC

steps, and handling these issues early through appropriate preprocessing ensures that the data is clean and reliable before modeling.

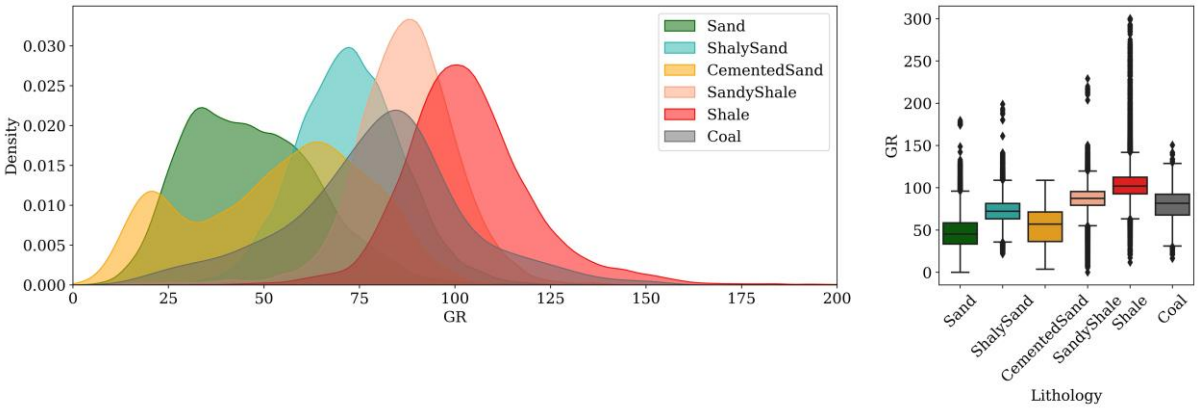

(a) **(b)**

Figure 2 – Distribution and Box plot of GR measurements across lithology types. (a) Distribution of GR for each lithology type. (b) Box plot summarizing central tendency, variability, and outliers for GR values in each lithology category.

Fig. 2 presents the distribution plot (Fig. 2 (a)) and box plot (Fig. 2 (b)) for the GR log across different lithologies. Upon examination of the distribution plot, it is evident that shale exhibits the highest GR values, followed by shaly-sand, as indicated by the peaks in the distribution curve. Conversely, sand and cemented sand exhibit relatively lower GR responses. This observation is further supported by the box plot, where shale and shaly-sand lithologies display higher median and upper quartile values compared to sand and cemented sand lithologies. Our findings align with geological knowledge, where shale formations typically exhibit elevated GR responses due to their higher clay content, while sand formations tend to display lower GR values. This alignment concludes the QC step of GR and confirms the reliability and accuracy of the GR log for subsequent analyses.

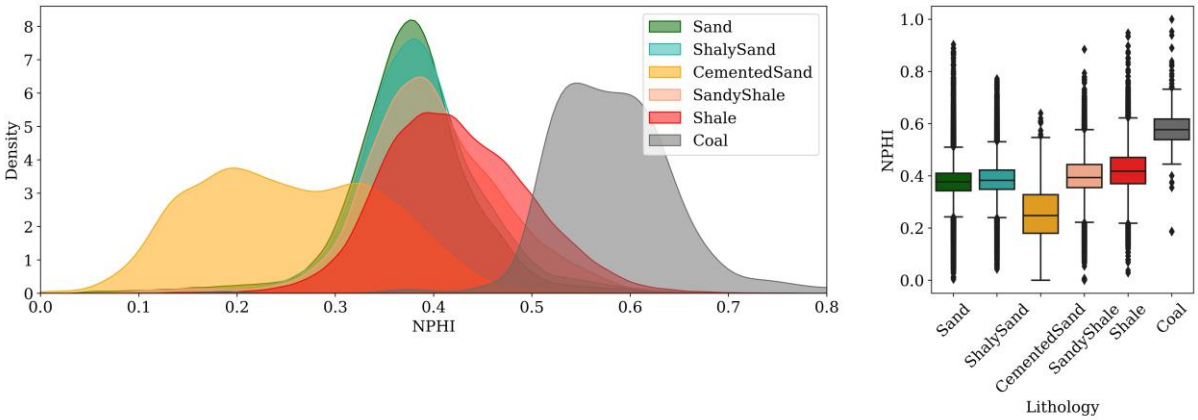

Figure 3 – Distribution and Box plot of NPHI measurements across lithology types. (a) Distribution of NPHI for each lithology type. (b) Box plot summarizing central tendency, variability, and outliers for NPHI values in each lithology category.

Similar to Fig. 2, Fig. 3 presents the distribution (Fig. 3 (a)) and box plot (Fig. 3 (b)) for the NPHI log across various lithologies. Our analysis reveals distinct and expected patterns: coal exhibits the highest NPHI values, while cemented-sand displays the lowest. Sand and shaly-sand demonstrate comparable responses to NPHI, with shaly-sand exhibiting slightly higher values as can be seen from the boxplot. Additionally, sandy-shale exhibits lower NPHI values compared to shale. These interpretations, derived from the distribution and box plot analyses, align closely with geological understanding and expectations.

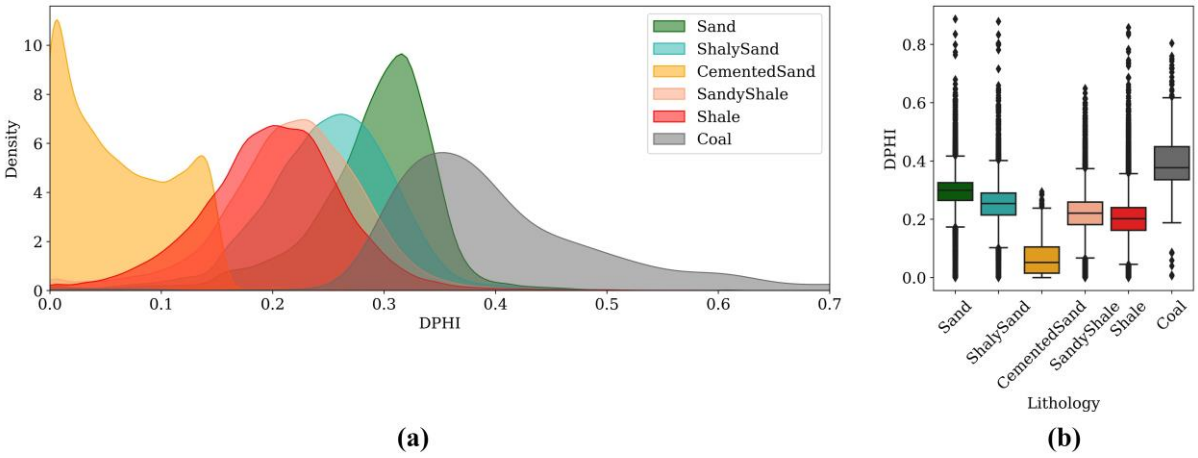

Figure 4 – Distribution and Box plot of DPHI measurements across lithology types. (a) Distribution of DPHI for each lithology type. (b) Box plot summarizing central tendency, variability, and outliers for DPHI values in each lithology category.

Finally Fig. 4 also depicts the same information like Fig. 2 and 3 for DPHI. Our analysis reveals that coal exhibits the highest DPHI values, while cemented-sand displays the lowest. Sand demonstrates higher DPHI values compared to shaly-sand. Additionally, sandy-shale exhibits higher DPHI values compared to shale. The observed variations in DPHI values across different lithologies closely align with geological understanding and expectations.

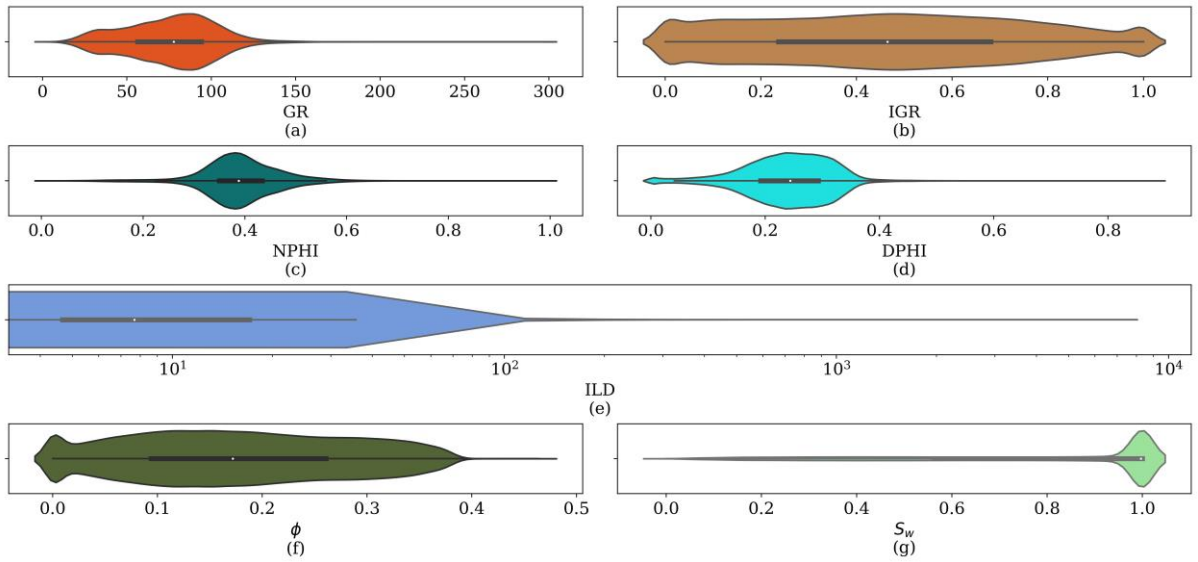

Figure 5 – Violin plot of Input logs (a)-(e) and Petrophysical parameters (f)-(g) proving statistical instights to the data. (a) Gamma Ray (b) Shaliness Index (c) Neutron Porosity (d) Density Porosity (e) Deep Resitivity (f) Porosity (ϕ), and (g) Water Saturation (S_w)

After analyzing the responses of various lithologies for different logs, we will now look into the statistical description of the input and output data using violin plots. A violin plot is a useful visualization tool that combines the benefits of a box plot and a kernel density plot, providing insights into the distribution and variability of data. As mentioned earlier, in our study, we have selected four basic logs as input to the model: GR, NPHI, DPHI, and ILD. Additionally, we introduced volume of shale (V_{sh}) derived from shaliness index (IGR) using the linear relationship between V_{sh} and IGR, as a feature-engineered independent variable (Hein et al., 2000; Wynne et al., 1995). Though the data provided by the Alberta Energy Regulator were already processed logs (Hein et al., 2000; Wynne et al., 1995), we still applied some preprocessing steps to enhance the performance of the DL model by removing the outliers in the GR log. Preprocessing applied to the GR values included despiking and setting a cutoff of 300 API for GR values. Fig. 5 presents the violin plot of input logs, GR, IGR, NPHI, DPHI, and ILD (a-e), as well as the output parameters, ϕ, and S_w (f-g). From Fig. 5, it can be observed that most GR values lie in the range of 10 to 150, while IGR ranges

from 0 to 1. NPHI mostly falls within the range of 0.2 to 0.6, and DPHI predominantly ranges from 0 to 0.4. ILD values are relatively low, typically ranging between 0 and 100, attributed to the high clay and pyrite content in Athabasca oil sands. Finally, the output values ϕ and S_w fall within the ranges of 0 to 0.4 and 0 to 1, respectively. This comprehensive statistical description, facilitated by violin plots, enhances our understanding of the dataset's distribution and variability, aiding in subsequent analyses and model development.

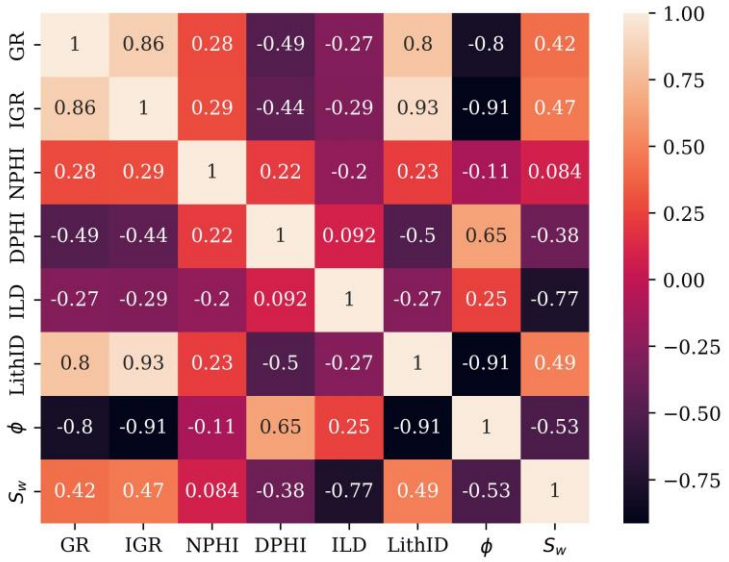

Figure 6 – Correlation Coefficients between Input logs and Output

Finally, in Fig. 6, we have also included a correlation heatmap plot between input logs and output parameters. This plot assists in comprehending the contribution of each input log to the estimation and prediction of the output parameters. It is evident from the plot that GR and IGR are most correlated with the lithology of the formation. For estimating ϕ, GR, IGR, and DPHI exhibit the highest correlation, while ILD shows the most correlation for estimating S_w. Overall, this plot provides deeper insights into the relationships between the inputs and outputs of the model, enhancing our understanding of the predictive processes involved.

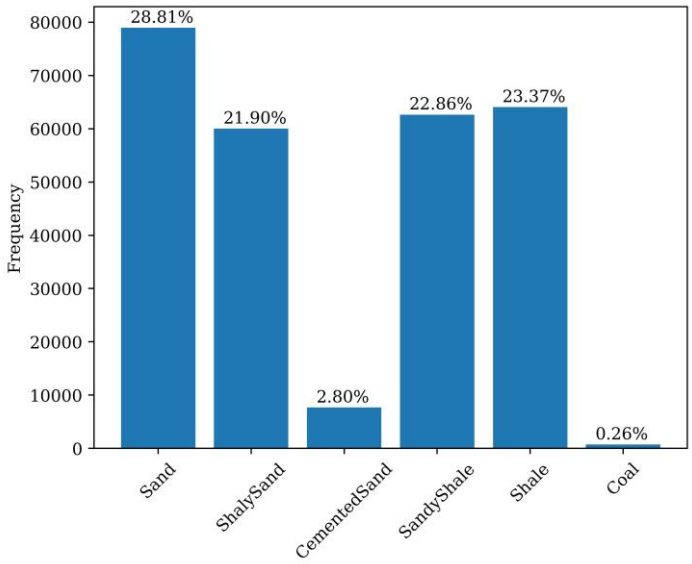

Figure 7 – Percentage distribution of lithology types in the dataset

Fig. 7 illustrates the percentage distribution of several lithology types in the dataset: Sand (28.81%), Shaly Sand (21.90%), Sandy Shale (22.86%), and Shale (23.37%) are the most common. Cemented Sand accounts for 2.80% and Coal for only 0.26%, making them the least represented. Detecting these under-represented lithologies accurately might be challenging due to their low percentage. We are going to address this issue in the methodology section, illustrating how our proposed approach beats standard models in identifying these less prevalent lithology classes.

In the field of DL, proper data scaling is paramount to effectively address complex tasks and unlock the full potential of neural networks (Glorot and Bengio, 2010). To this end, we applied the StandardScaler (Pedregosa et al., 2011) to normalize attributes such as GR, NPHI, DPHI, and ILD, ensuring these independent variables possess a mean of zero and a standard deviation of one. This standardization procedure equalizes the contribution of each attribute within DL models, mitigating the dominance of features with larger scales, thereby promoting model convergence and enhancing overall performance. Although in manual log analysis, GR, NPHI, and DPHI are scaled linearly while ILD is scaled logarithmically, such

scaling is not required in a DL approach. The rationale for scaling in log analysis differs from that of DL; in log analysis, scaling is primarily for visualization purposes, as our eyes are responsive to observed patterns, hence logarithmic scaling of ILD becomes necessary. However, in DL, the machine processes both patterns and numerical values, making scaling for visualization purposes unnecessary. As mentioned above, in DL, scaling is primarily aimed at facilitating faster convergence and preventing any single attribute from overshadowing others. Additionally, IGR, a feature-engineered independent variable, was also subjected to the same scaling treatment for consistency and optimal model training (Wynne et al., 1995). We adopted patching as an approach to generate the dataset, where instead of considering the entire well log as a single instance, we divided it into smaller patches. This decision was motivated by the aim to augment the dataset size, a strategy advocated by Alaudah et al., 2019. Following this, we proceeded to segment the well logs into smaller patches for model training. Our empirical findings indicated that a patch size of 150 yielded optimal results. Notably, we employed a non-overlapping approach in generating these patches (Alaudah et al., 2019). Each individual patch was linked to its corresponding dependent variables, encompassing Lithology, ϕ, and S_w. To evaluate the model's performance on previously unseen data, we implemented two distinct splitting strategies. Firstly, we created a blind set by randomly selecting 10 wells from the dataset. This separation allowed us to assess the model's performance into its generalization capabilities. Secondly, to assess the effectiveness of LoRA (Hu et al., 2022), we again isolated 100 additional random wells. The remaining wells underwent a conventional random 80:20 split, dividing them into training and testing subsets, enabling us to gauge the model's performance while training the model. With the use of these data-splitting strategies, our dataset allowed for a thorough evaluation of the model's predictive ability in a variety of scenarios and domains.

3. Methodologies

In this section, we present a detailed account of the methodology employed in this study to predict lithology and estimate petrophysical parameters accurately. We discuss three primary components of our approach, each contributing to the overall effectiveness of our model. The subsections will elaborate on the ViT model, ARViT model, and the LoRA technique, shedding light on their respective roles in our research.

3.1. Vision Transformer (ViT)

We introduce our methodology centered on transformers, featuring a self-attention mechanism (Vaswani et al., 2017) embedded within a ViT model (Dosovitskiy et al., 2021). Self-attention enables each data point within the well-log curves to weigh its importance in relation to other depths or data points in the same curve, helping in easy identification of geological features and patterns. Our ViT model (Fig. 7) is composed of two principal components: the ViT Encoder and the Prediction Head. Within the ViT encoder, we initially transform the well log patches into multiple sub-patches, an operation conducted horizontally to encompass all features across the patch, effectively covering 150 depth points. These sub-patches undergo a sequence of transformations, commencing with Layer Normalization (LayerNorm) (Ba et al., 2015; Xiong et al., 2020), followed by a Fully Connected (FC) Layer and another LayerNorm. Layer normalization standardizes the activations of each layer, ensuring consistent scaling and aiding in stabilizing the training process, which is beneficial when dealing with diverse and varying well log data. We also augment the output of LayerNorm by adding positional encoding, leveraging sine-cosine positional embedding (Ke et al., 2021; Vaswani et al., 2017) to impart positional information to each patch (Dosovitskiy et al., 2021). Subsequently, the linear projection of sub-patches is fed into Transformer layers, featuring residual (He et al., 2016) self-attention mechanisms and feed-forward layers.

Self-attention enables the network to dynamically weigh the importance of each input element relative to others in the sequence, enhancing it's ability to capture contextual dependencies. The feed-forward layer uses LayerNorm, Linear Layer, activation function, and another Linear Layer.

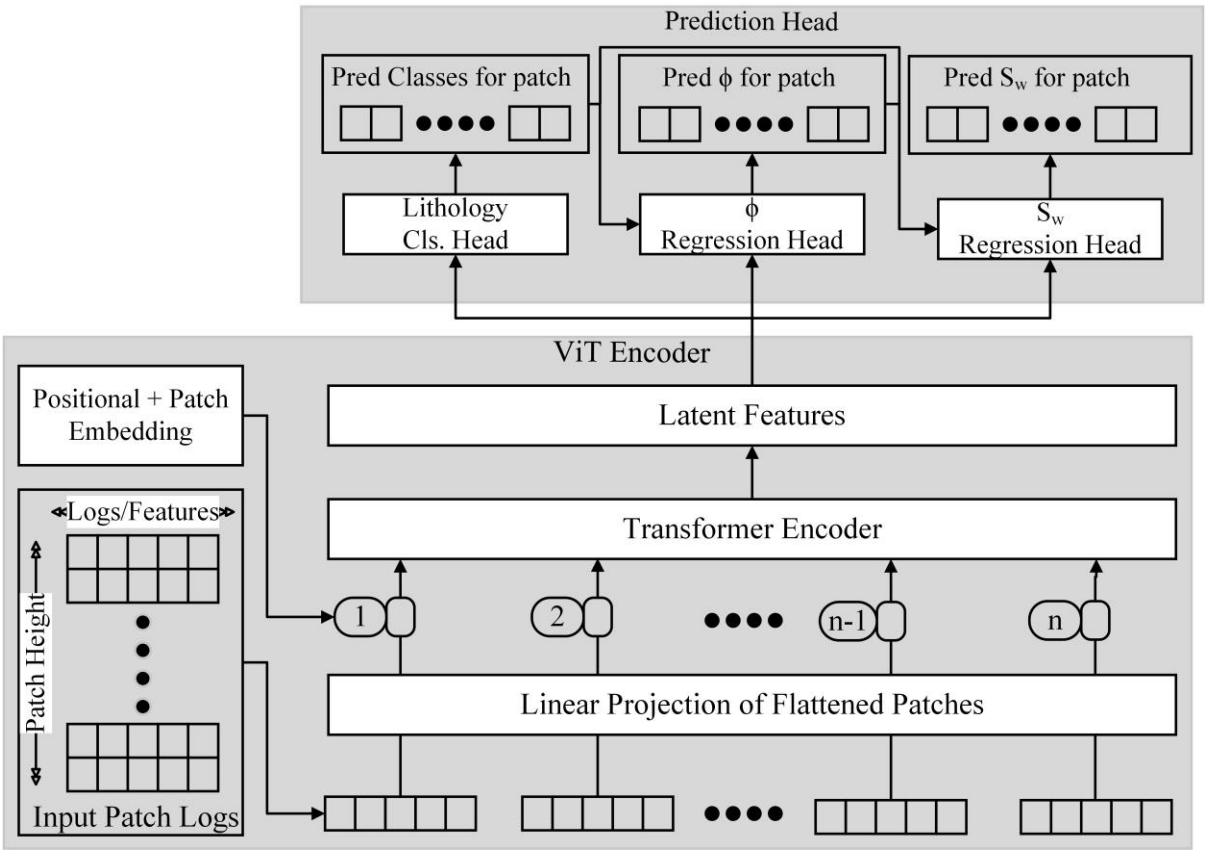

Figure 8 – Workflow Diagram of the ViT Model. The ViT workflow comprises two main components: the ViT Encoder and the Prediction Head, each contributing to the model's comprehensive well-log understanding.

Following the ViT Encoder, a Prediction Head is introduced, designed to accommodate multitasking. Comprising three distinct sub-heads, it helps in lithology classification, ϕ prediction, and S_w prediction as separate tasks. Each sub-head incorporates two FC Layers, sandwiched with LayerNorm and an activation function. The architecture of the Prediction Head mirrors conventional interpretation procedures, maintaining fidelity to established

industry practices. The latent features generated by the ViT Encoder are passed through the Lithology Classification Head, with the output of this head, in conjunction with the latent features of the ViT, proceeding to the ϕ Regression Head. Finally, for the prediction of S_w, input to the S_w Regression Head includes the output of the ViT Encoder, the Lithology Classification Head, and the ϕ Regression Head. The input logs remain consistent across all tasks, underscoring the architecture's aim to jointly optimize three distinct tasks utilizing identical models and input spaces. Notably, within the ViT model architecture, ϕ indirectly integrates the latent representation of lithology as input. Likewise, S_w indirectly incorporates the latent representations of lithology and ϕ alongside the existing model inputs (Fig. 8). This model architecture enables simultaneous performance across multiple geological prediction tasks, closely mirroring the workflows of traditional interpretation methods.

3.2.AutoRegressive ViT (ARViT)

Subsequently, we introduce our proposed approach, referred to as ARViT (Fig. 8 (a)), extending the ViT model described earlier. While the encoder block remains consistent with the previously outlined ViT structure, ARViT incorporates a distinctive prediction encoder block. The prediction encoder block comprises FC Layers, succeeded by LayerNorm and an Activation function. The output of this prediction encoder subsequently traverses a masking layer. The output from the masking layer is then fused with the output from the ViT Encoder, facilitated by a Merge layer comprising FC Layers. Ultimately, the output from the Merge layer is directed to the Prediction Head.

The Prediction Head in ARViT maintains consistency with its ViT counterpart, with one major difference: in ARViT, predictions are made at a pointwise level rather than for the entire patch. ARViT operates by first predicting lithology, ϕ, and S_w for the initial depth location within the patch, denoted as *step-1*. The predicted lithology probability, coupled

with, ϕ, and S_w predictions, serves as input to the prediction encoder. Using this input, ARViT computes predicted probabilities for the subsequent depth location, denoted as *step 2*. To enforce causal relationships within the model, we introduce causality via masking (Lin et al., 2017). Specifically, when creating a mask for *step-s*, the mask for all depth points is assigned a value of 1 until *step s-1*, with the mask for remainder depth points set to 0. This mask is then applied to the features extracted from the activation layer of the prediction encoder. By doing so, all values beyond *step s-1* are effectively masked, preventing information leakage and ensuring that predictions for each depth location depend solely on prior steps. To predict the s^{th} location, a cumulative aggregation of predictions up to *step s-1* is employed, serving as input for the prediction encoder. This auto-regressive mechanism within ARViT enables accurate pointwise predictions while preserving causal relationships, enhancing the model's interpretability and performance.

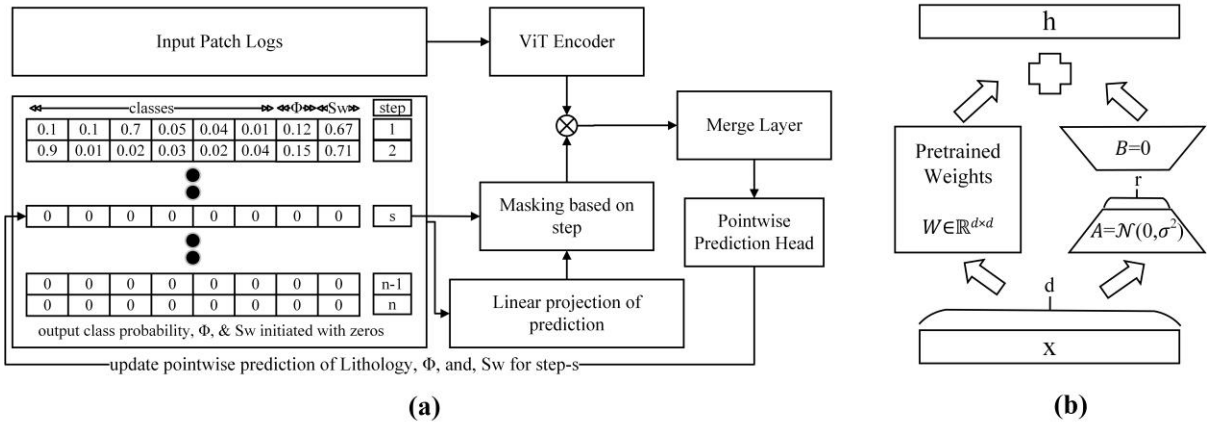

Figure 9 – Workflow Diagram of the (a) ARViT Model and (b) LoRA. (a) The ARViT workflow begins with input patches processed through the ViT Encoder and an output vector initialized with zeroes, processed through the Prediction Encoder. The merged outputs are then directed to the Prediction Head, which iteratively updates the output zeroes initialized values, enabling precise pointwise predictions. (b) Reparameterization of Weights using LoRA

Incorporating autoregressive methods within a ViT model allows for sequential prediction of lithology and petrophysical parameters, enhancing the model's contextual awareness. By employing this autoregressive approach, the ViT sequentially processes output, utilizing prior predictions as a context for subsequent depth levels. This methodology ensures that each prediction for lithological and petrophysical parameters builds upon the previously established context, maintaining consistency and reducing deviations from one depth to the next. Essentially, when predicting the characteristics at a specific depth, the model uses all preceding outputs, thus integrating earlier petrophysical parameters and lithology to inform and refine its current predictions. This step-wise, context-aware processing significantly improves the accuracy and reliability of lithology and petrophysical parameter estimation as compared to other models like ANN, LSTM, and ViT.

3.3.Low Rank Adaptation (LoRA)

Subsequently, we introduce the concept of LoRA. LoRA entails a strategic restructuring of weight matrices within specific layers, as shown in Fig. 9 (b), to attain a lower rank compared to their original configurations (Hu et al., 2022). This is accomplished by decomposing these weight matrices into two lower-dimensional matrices, resulting in a reduction in both the model's trainable parameter counts and overall complexity.

For LoRA to be applied to a weight matrix W_0, we put a constraint to the update of that pre-trained weight matrix $W_0 \in R^{d\times k}$ by representing it using a low-rank decomposition, $W_0 + \Delta W = W_0 + BA$, where $B \in R^{d\times r}$, $A \in R^{r\times k}$, and $r \ll min(d,k)$. During the training process, W_0 remains fixed without receiving gradient updates, while A and B contain trainable parameters. It's important to note that both W_0 and $\Delta W = BA$ are multiplied with the same input, and their respective output vectors are combined element-wise (Hu et al., 2022).

For a given input x, the modified forward pass is expressed as:

$$h = W_0 x + \Delta W x = W_0 x + BAx, \quad (1)$$

where W_0 is the pre-trained freezed-weight matrix of the network, ΔW is the update to the weight matrix through low-rank decomposition, A and B contains the trainable weight parameters for LoRA fine-tuning and are essentially the decomposed matrices representing the low-rank approximation, x is the input vector and h is the output vector after the application of LoRA. Notably, the application of LoRA was selectively targeted, affecting only a subset of layers within our architecture.

3.4.Model Hyperparameters

In this study, ARViT model was configured with several hyperparameters to optimize its performance. The model features a feedforward MLP dimension of 128, a single encoder transformer layer, and 4 number of attention heads, with a hidden dimension set at 150 and a ReLU activation function. The same configurations was used for the ViT model. The auto-regressor's hidden layer sizes are also defined as 150. The choice of 150 as hidden dimesion was due to the fact that we are using an input of patch size of 150 and want the prediction for lithology and petrophysical parameters for these 150 depth points. Additionally, LoRA technique was employed, with a rank of 16 to enhance the model's efficiency and adaptability during fine-tuning. The training process consisted of 200 epochs, utilizing a learning rate of 0.001 and a batch size of 64, with the Adam optimizer selected for optimizing the model’s parameter for best performance.

4. Experiments and Results

In this research, we commenced by constructing a baseline model using ANN. This foundational model was structured with three hidden layers, each containing 10 nodes. Following these hidden layers, we applied the same prediction head, as detailed in section 3.

This baseline model serves as the reference point for evaluating the effectiveness of our proposed approaches. Additionally, we conducted a comparative analysis with the LSTM model, which features an encoder and a prediction head. The encoder of the LSTM model consists of a single LSTM layer. In our experimental setup, we standardized the optimization and loss functions across all models.

The ADAM optimizer was employed uniformly for all models (Kingma and Ba, 2015). The ADAM optimizer is an adaptive learning rate optimization algorithm that combines the advantages of two other extensions of stochastic gradient descent: AdaGrad (Adaptive Gradient) (Duchi et al., 2011) and RMSProp (Root Mean Squared Propagation) (Elshamy et al., 2023). ADAM optimizer adjusts the learning rates of individual parameters leading to faster convergence and improved performance in training complex models (Anggara et al., 2023).

To address the distinct objectives within our multi-task framework, we employed a combination of loss functions. Specifically, we applied cross-entropy loss for the lithology prediction task, while for the regression tasks encompassing ϕ and S_w, Mean Squared Error (MSE) Loss was utilized. Cross-entropy loss emphasizes the difference between predicted and actual categorical values of lithology, while MSE loss focuses on minimizing the squared differences between predicted and actual continuous values of ϕ and S_w, both serving as key metrics to guide model training. We incorporated class weights in the cross-entropy loss to improve the accuracy of identifying the two classes present in low percentage, Cemented Sand and Coal. In our multi-task learning model, it was imperative to balance the loss contributions from the three prediction heads, each catering to a distinct prediction task. To achieve this balance, we introduced weighting factors denoted as $\lambda_l, \lambda_\phi, and\, \lambda_{sw}$ for

lithology, ϕ, and S_w loss weighting. The overall loss was calculated using the formula given below

$$Loss = (\lambda_l * Loss_l) + (\lambda_\phi * Loss_\phi) + (\lambda_{sw} * Loss_{S_w}), \quad (2)$$

where $Loss_l$, $Loss_\phi$, and $Loss_{S_w}$ is the lithology, porosity and water saturation loss, respectively. $\lambda_l, \lambda_\phi, and\ \lambda_{S_w}$ is the weight applied to lithology, porosity, and water saturation loss. $Loss_l, Loss_\phi\ and\ Loss_{sw}$ are loss calculated from lithology, ϕ, and S_w head. We found that the value of $\lambda_l, \lambda_\phi, and\ \lambda_{S_w}$ set at 1, 10, 20 gave us the best performance. These weightings made sure that the loss associated with each prediction task was appropriately scaled, reflecting their relative importance within the multi-task learning context.

Maintaining consistency, the learning rate (LR) across all models was set at 0.001. To ensure the convergence of our models and mitigate overfitting, we imposed a maximum training duration, limiting the number of epochs to 200. Additionally, a stopping criterion was instituted: if the validation performance did not exhibit improvement over 10 consecutive epochs, the training process was automatically terminated. NVIDIA's Quadro P4000 graphics processing unit (GPU), boasting 8 GB of dedicated memory, was utilized to accelerate computations, ensuring efficient processing for lithology and petrophysical parameter predictions. These standardized settings contributed to a fair and reliable evaluation of our models across various experiments.

Further in this section, we present the outcomes of our model training efforts in Table 1. We initiated our study by training our baseline model, ANN. On the blind set, this model demonstrated an accuracy of 73.18% for Lithology prediction, MSE values of 0.0007 for ϕ prediction, and 0.022 for S_w prediction.

Table 1. Model Performance Comparison on Lithology, ϕ, and S_w Prediction on blind set.

Model Name	Lithology		ϕ		S_w	
	Accuracy	**F1-Score**	**MSE**	**MAE**	**MSE**	**MAE**
ANN (Baseline)	73.18	43.16	0.0007	0.021	0.022	0.131
LSTM	89.80	67.50	0.0010	0.023	0.010	0.071
ViT	93.23	80.83	0.0005	0.017	0.016	0.075
AutoRegressive ViT	**96.51**	**86.83**	**0.0004**	**0.016**	**0.005**	**0.046**

To provide a comprehensive evaluation of our model's performance, we conducted a comparative analysis with LSTM. On the blind set, LSTM achieved an accuracy of approximately 89.80% for Lithology prediction. In regression tasks, LSTM attained MSE values of 0.001 for ϕ and 0.010 for S_w prediction. Subsequently, we introduced the ViT model into our study. On the blind set, the ViT model delivered impressive results with an accuracy of 93.23% for Lithology prediction. For regression tasks, it demonstrated MSE values of 0.0005 for ϕ, and 0.016 for S_w prediction. Finally, we introduced our proposed methodology, ARViT, which achieved a Lithology prediction accuracy of 96.51% on the blind set. In regression tasks, ARViT exhibited MSE values of 0.0004 for ϕ and 0.005 for S_w prediction. These results underscore the progressive improvements in model performance as we advanced through our experimental iterations, highlighting the potential and effectiveness of our proposed ARViT model. To assess our ARViT model's performance better, we also accessed the model's performance using F1-Score for lithology prediction. F1-Score came out to be 43.16%, 67.50%, 80.83% and 86.83% for ANN, LSTM, ViT and ARViT respectively for blind set.

Table 2. Model Performance Comparison on each Lithology types prediction on blind set.

Performance	**Model**	**Lithological Class Performance (%)**

Metrics	Name	Sand	Shaly Sand	Cemented Sand	Sandy Shale	Shale	Coal
Recall	**ANN**	99.05	95.68	3.14	96.27	6.47	1.92
	LSTM	98.24	96.40	76.58	91.49	77.15	2.36
	ViT	93.37	91.76	92.22	93.64	96.24	92.37
	ARViT	97.64	**96.71**	**94.34**	**97.54**	**97.69**	**96.15**
Precision	**ANN**	85.66	86.7	0.81	57.12	3.36	0.39
	LSTM	86.79	87.84	39.28	84.40	86.64	0.68
	ViT	92.83	92.16	50.38	90.59	87.1	35.53
	ARViT	**99.27**	**98.71**	**62.12**	**99.07**	**98.05**	**37.3**
F1-Score	**ANN**	91.87	90.97	1.29	71.70	2.48	0.65
	LSTM	92.16	91.92	51.93	87.11	81.62	1.06
	ViT	93.10	91.96	65.16	92.09	91.44	51.32
	ARViT	**98.45**	**97.70**	**74.91**	**98.30**	**97.87**	**53.75**

Table 2 compares the performance of several models (ANN, LSTM, ViT, and ARViT) in identifying lithology based on precision, recall, and F1-score for various lithological classes. The ARViT model shows better performance in distinguishing Sand, Shaly Sand, Sandy Shale, and Shale, with accuracy, recall, and F1-scores above those of other models. ANN and LSTM showed very poor performance in detecting Coal and Cemented Sand due to their low-representation in the study area. ViT showed a boost in detecting these under-represented lithologies due to the use of self-attention. Finally, ARViT demonstrates superior effectiveness in detecting under-represented lithology in our study area, Cemented Sand and

Coal, when compared with other models. In conclusion, ARViT surpasses all other models in detecting lithology and calculating ϕ and S_w across all three objectives.

5. Discussions

In the preceding section, we have provided an extensive account of our experimental results (Table 1). Notably, our findings consistently demonstrated better performance of the ARViT model. In Fig. 10, 11, 12, 13, and 14, we present a comparative result of the proposed ARViT model between the Ground Truth (GT), which represents the actual observed data, and the prediction generated by ARViT model, along with the prediction from ANN, LSTM, and ViT for comparision. The result is shown for 5 different wells with Unique Well Identifier (UWI) number *00-12-04-072-06W4-0, 00-10-21-081-24W4-0, 00-08-09-079-05W4-0, 00-07-28-068-09W4-0,* and *00-06-22-069-05W4-0*. The UWI serves as a unique identifier for each well in the dataset.

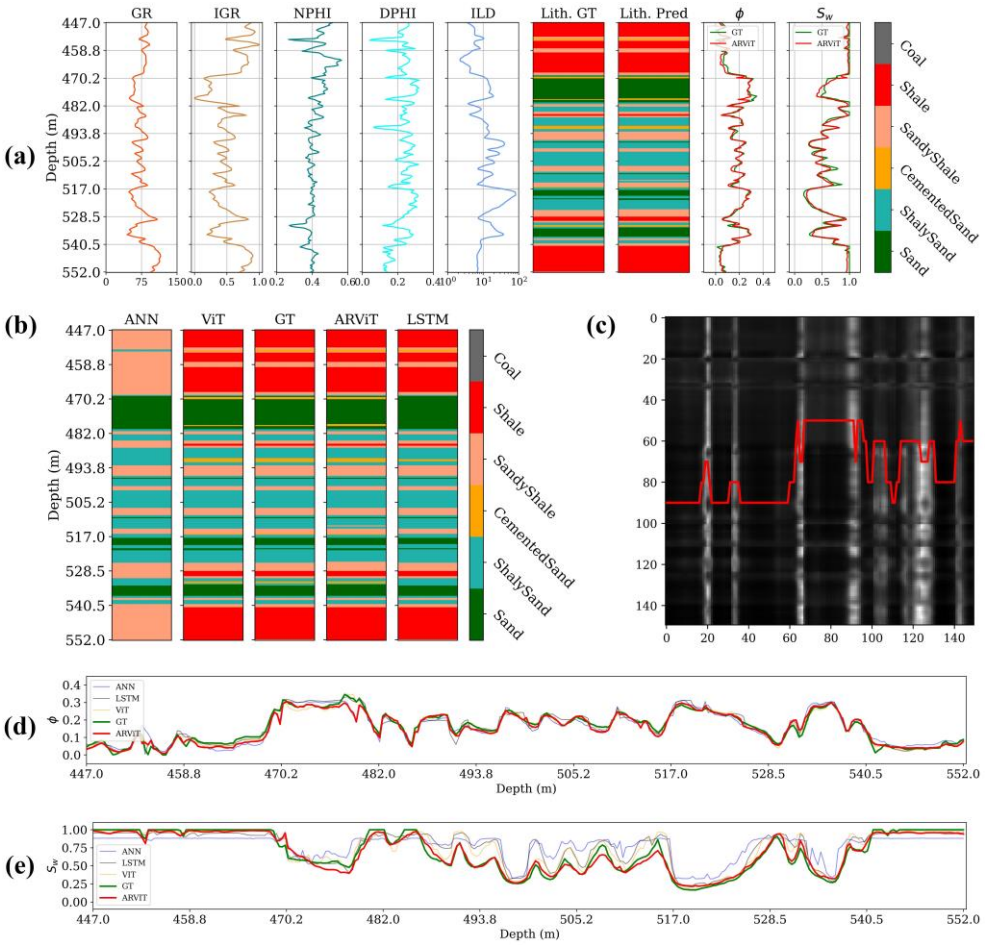

Figure 10 – Results on well with UWI 00-12-04-072-06W4-0 (a) Results of proposed ARViT Model. It illustrates the input log (first five panel from left) along with the predictions (last three panel) obtained from ARViT model. (b) Comparative analysis of lithology prediction from different models. Leftmost panel shows the prediction from ANN, followed by ViT. The middle panel shows the true lithology, GT. The second last panel shows the prediction from ARViT followed by LSTM. (c) Attention Map obtained from ViT model illustrating Self-Attention Mechanism. The red line shows the class change for depth range 447 - 484.5 m. Areas with the same class exhibit consistent attention weight patterns, while attention weights change when there's a transition in class. (d) Porosity (ϕ) and (e) Water Saturation (S_w) estimation from different models.

Fig 10-14 (a) shows the ARViT model's prediction and comparison with GT on five different wells. This visual comparison with GT aids in evaluating the model's performance, revealing a close alignment between ARViT's predictions and GT. Occasional deviations from GT are

also observed at few zones, indicating some opportunities for further improvement. For instance, in Fig. 10 (a), a misclassification is noted at 492.65 meters, where the ARViT model predicts a thin sandy-shale zone instead of shaly-sand. At about 471 meters, ARViT model overestimated the cemented sand zone. There are very few zones where we see minor misalignnment in ϕ and S_w estimation. Overall, predictions of Lithology, ϕ and S_w exhibit close alignment with GT, with minor deviations observed. Fig. 11 (a) shows predominantly close alignment with GT, with minor deviations in Lithology, ϕ and S_w predictions noted between 468-472, 454.8-455.8 and 445-453 meters. We observe that the ARViT overestimated the coal identification at 464 and 470 meters. Apart from these zones, we see an overall alignment of ARViT's prediction with GT. In Fig. 12 (a), lithology prediction is generally accurate, with a minor misclassification at 229 and 232 meters where ARViT missed thin shaly sand zone. Apart from this lithological misclassification, we see close alignment of petrophysical properties estimation with GT.In Fig. 13 (a), while most lithology predictions align with GT, an overestimation in cemented-sand and sand is observed at 654 and 700 meters respectively. Minor deviations in ϕ and S_w predictions are also noted for this zone and the zone above it. Similarly, in Fig 14 (a), we see good alignment of ARViT's prediction with that of GT, with some minor deviation in S_w estimation. Overall, the model demonstrates good performance in lithology prediction, with ϕ prediction exhibiting minor deviations. Among the three predictions (lithology, ϕ, and S_w), lithology shows the best alignment with GT, whereas S_w exhibits slightly more deviation compared to ϕ.

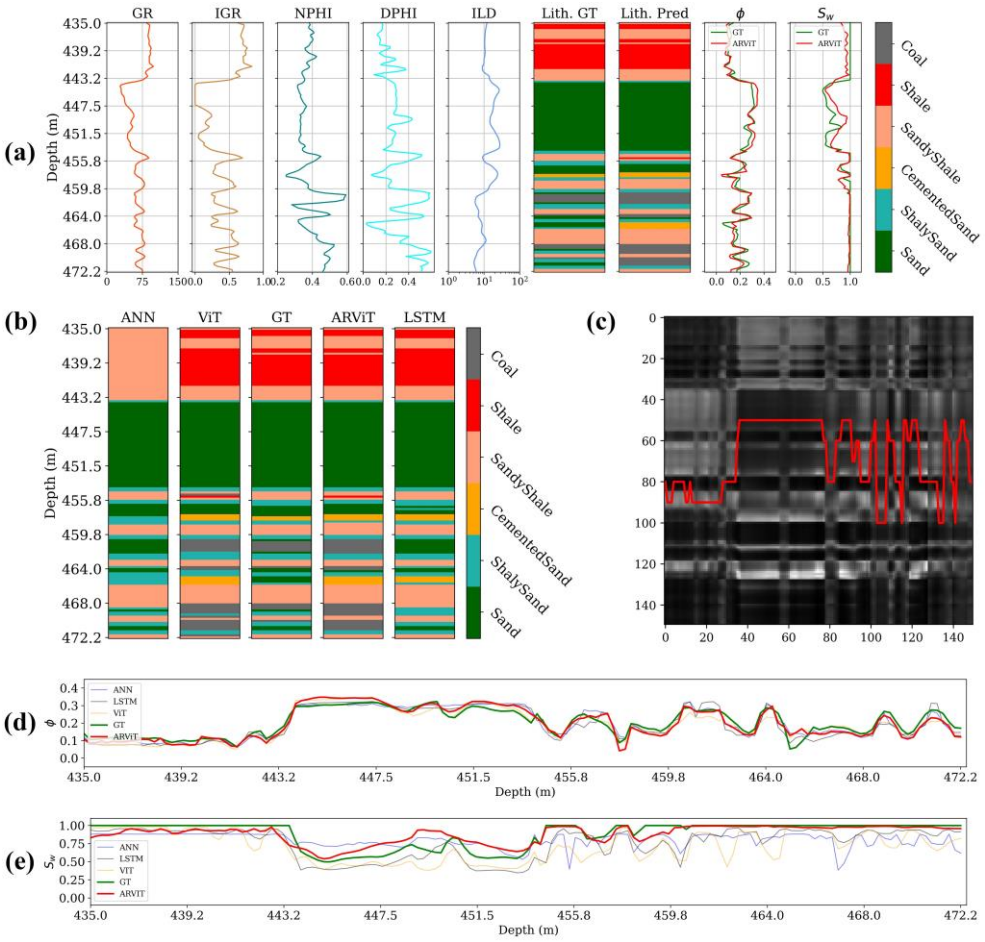

Figure 11 – Results on well with UWI 00-10-21-081-24W4-0 (a) Results of proposed ARViT Model. (b) Comparative analysis of lithology prediction from different models. (c) Attention Map obtained from ViT model illustrating Self-Attention Mechanism for depth range 435 – 472.2 m. (d) Porosity (ϕ) and (e) Water Saturation (S_w) estimation from different models. All the properties of the figure are same as the Fig. 10.

To gain deeper insights into the inner workings of the self-attention mechanism, we have incorporated an attention map for each well in Fig. 10-14 (c), a valuable tool that offers us a visual representation of how self-attention operates within the model. Upon careful examination of the attention map, a compelling pattern emerges. We observe that regions within the same lithological class exhibit uniform attention weights. However, these attention weights dynamically change whenever there is a transition between lithological classes. This observation is of paramount significance, as it underlines how the self-attention mechanism

effectively captures contextual dependencies and discriminates between lithological categories. By visualizing these attention maps, we gain valuable intuition into the model's decision-making process and its capacity to recognize lithological patterns, further validating the use of self-attention mechanism in the proposed models for lithology prediction.

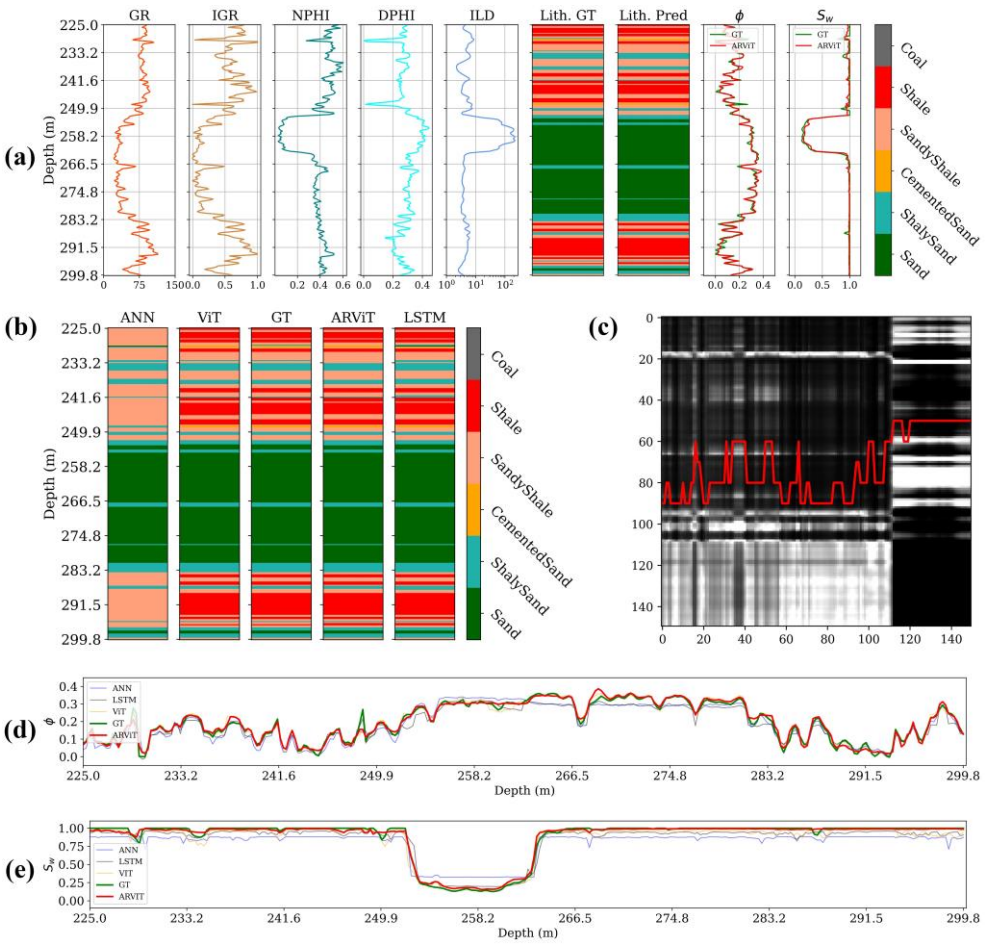

Figure 12 – Results on well with UWI 00-08-09-079-05W4-0 (a) Results of proposed ARViT Model. (b) Comparative analysis of lithology prediction from different models. (c) Attention Map obtained from ViT model illustrating Self-Attention Mechanism for depth range 225 – 262.4 m. (d) Porosity (ϕ) and (e) Water Saturation (S_w) estimation from different models. All the properties of the figure are same as the Fig. 10.

In Figures 10-14 (c), a comparative analysis of lithology predictions from various models (ANN, LSTM, ViT, and ARViT) and GT is presented. These figures offer valuable insights

into the progressive improvement in model performance from ANN to LSTM to ViT and ultimately to ARViT. Upon examining the lithological predictions of different models, it becomes evident that ANN exhibits the poorest performance, consistently struggling to identify shale zones and often misclassifying them as sandy-shale zones (Fig. 10-14 (b)). ANN also struggles in recognizing cemented-sand and coal. It often misclassifies coal as sand due to low GR value (Fig. 11 (b)). LSTM also suffers with the misclassification of coal as sand and sandy-shale (Fig. 11 (b)). It also struggles to identify cemented-sand (Fig. 12 (b)). In Figures 10 (b), 11 (b) and 13 (b), it is observed that LSTM encounters difficulties in identifying thin zones and may struggle in certain locations. In Figures 11(b), LSTM struggles to detect areas containing coal. On the other hand, ViT and ARViT are able to classify coal and cemented-sand better than ANN and LSTM. Though ViT faces issues in coaly zones, showing higher overestimation compared to ARViT. In conclusion, ARViT, the proposed model, outperforms ANN, LSTM, and ViT in lithology prediction by exhibiting the lowest misclassification rate and highest alignment with GT.

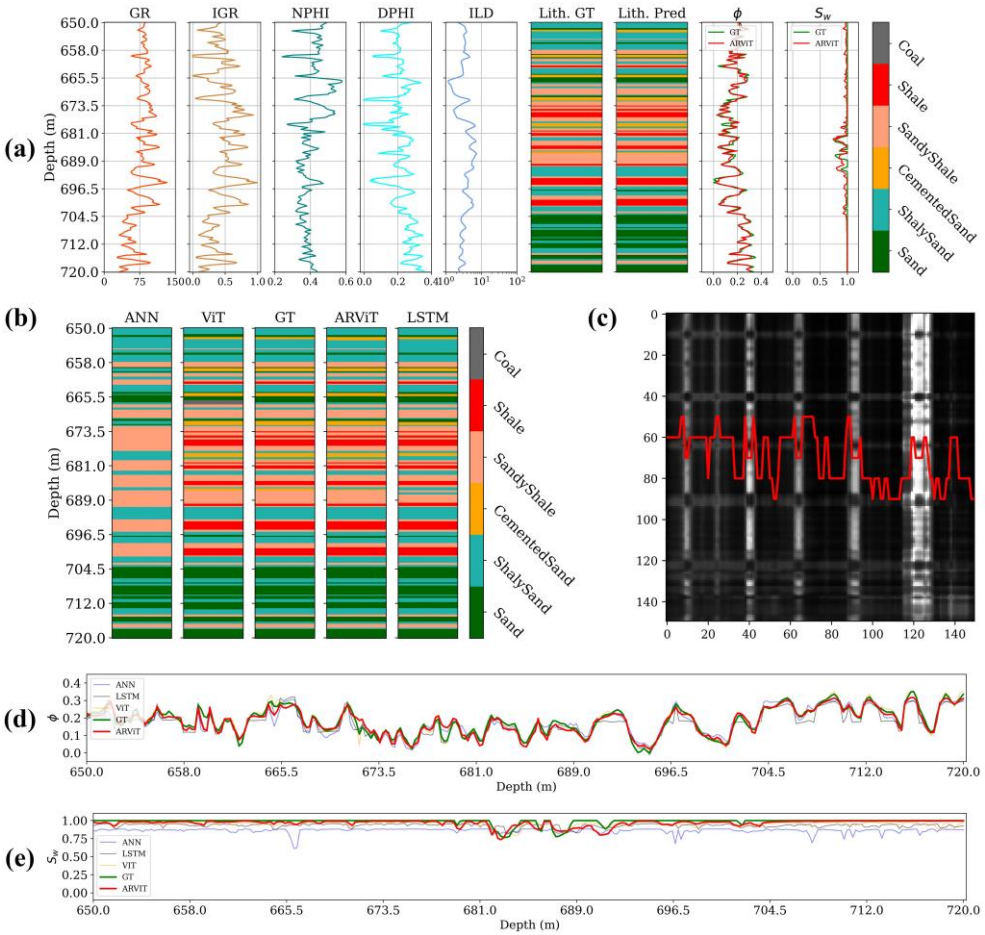

Figure 13 – Results on well with UWI 00-07-28-068-09W4-0 (a) Results of proposed ARViT Model. (b) Comparative analysis of lithology prediction from different models. (c) Attention Map obtained from ViT model illustrating Self-Attention Mechanism for depth range 650 – 685 m. (d) Porosity (ϕ) and (e) Water Saturation (S_w) estimation from different models. All the properties of the figure are same as the Fig. 10

Figures 10-14 also illustrates comparison of ϕ (Fig. 10-14 (d)) and S_w (Fig. 10-14 (e)) predictions with GT. Similar to previous figures, these plots offer valuable insights into the progressive enhancement of model performance from ANN to LSTM to ViT and ultimately to ARViT. It is evident from these figures that LSTM exhibits the poorest performance in ϕ estimation, followed by ANN, ViT, and the best model, ARViT. Across all blind wells, ARViT demonstrates close alignment of ϕ predictions with GT, with minor deviations observed in certain zones, outperforming ANN, LSTM, and ViT. Regarding S_w, ANN

displays the highest deviation, followed by ViT. LSTM demonstrates comparatively better performance in S_w estimation compared to ANN and ViT. The improved performance of LSTM in S_w estimation can be attributed to its sequential data processing nature. As S_w remains predominantly constant and changes in the presence of potential hydrocarbons, the sequential processing nature of LSTM enables it to remember previous time step values, aiding in predicting subsequent values. Similarly, the sequential processing, enhanced by auto-regression and self-attention mechanisms in ARViT, contributes to its superiority over LSTM in water saturation prediction. Thus, it is evident that ARViT outperforms all other models in both ϕ and S_w estimation tasks.

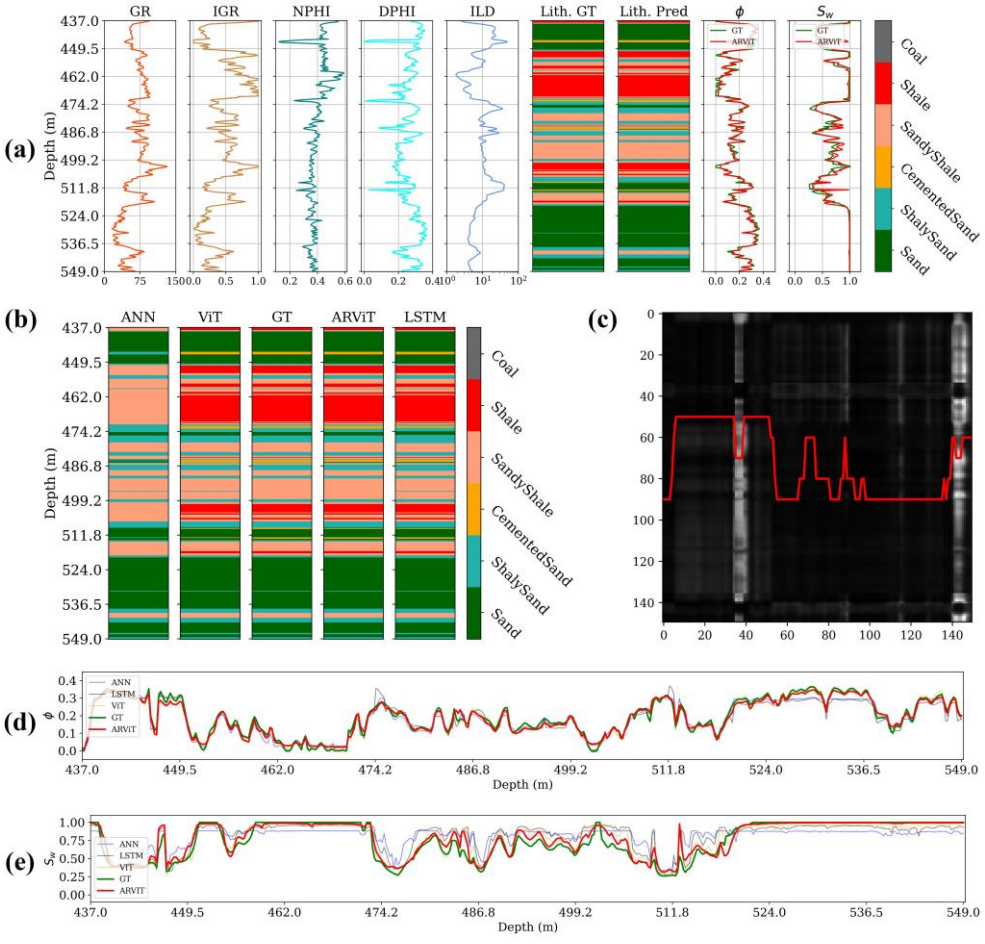

Figure 14 – Results on well with UWI 00-06-22-069-05W4-0 (a) Results of proposed ARViT Model. (b) Comparative analysis of lithology prediction from different models. (c) Attention Map obtained

from ViT model illustrating Self-Attention Mechanism for depth range 650 – 685 m. (d) Porosity (ϕ) and (e) Water Saturation (S_w) estimation from different models. All the properties of the figure are same as the Fig. 10

Fig. 15 and 16 presents a cross plot that serves as a visual comparison between the model's predicted values (ANN, LSTM, ViT, and ARViT) and the actual GT values for ϕ, and S_w. We illustrate crossplots for each model discussed in this study (Fig. 15 and 16). Fig. 15 displays the crossplot for ϕ, while Fig. 16 shows the crossplot for S_w. LSTM demonstrates the lowest performance in estimating ϕ (r^2 = 0.75, Pearson coefficient = 0.91) (Fig. 15 (b)), followed by improved performance in ANN (r^2 = 0.90, Pearson coefficient = 0.96) (Fig. 15 (a)). ViT exhibits a slight performance increase over ANN in estimating ϕ (r^2 = 0.94, Pearson coefficient = 0.98) (Fig. 15 (c)), while ARViT achieves the best performance (r^2 = 0.95, Pearson coefficient = 0.97) (Fig. 15 (d)). Conversely, ANN demonstrates the poorest performance in estimating S_w (r^2 = 0.55, Pearson coefficient = 0.77) (Fig. 16 (a)), followed by a performance boost in ViT (r^2 = 0.68, Pearson coefficient = 0.85) (Fig. 16 (c)), and then LSTM (r^2 = 0.77, Pearson coefficient = 0.88) (Fig. 16 (b)). ARViT achieves the highest performance in estimating S_w (r^2 = 0.93, Pearson coefficient = 0.97) (Fig. 16 (d)). Fig. 15 and 16 offers a concise yet insightful view of the different model's performance in estimating these critical petrophysical parameters. When data points align closely along the red diagonal line, it signifies accurate predictions, indicating that the model's estimation closely matches the GT values. This visual assessment along with correlation value provides a valuable snapshot of the model's overall predictive capability and its capacity to capture the underlying relationships between ϕ, and S_w.

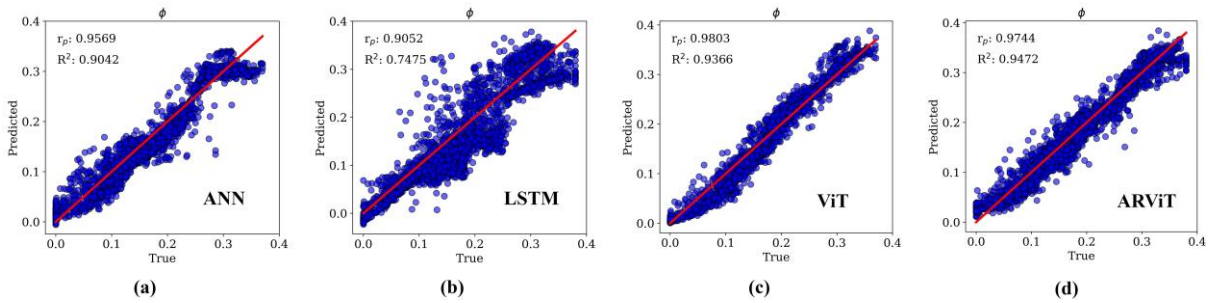

Figure 15 – Cross-Plots between True and Predicted Porosity from various models along with pearson coefficient and r2 score. (a) ANN, (b) LSTM, (c) ViT, and (d) ARViT. These cross-plots offer insights into the performance and accuracy of each model in estimating porosity, facilitating comparative analysis and model evaluation.

In this discussion section, we also explore the critical role that LoRA plays in optimizing our model, especially in situations where the availability of labelled datasets and computational resources is constrained. In situations where dataset sizes are relatively small, adopting transfer learning practices becomes a natural choice. Within the scope of this research, we specifically introduced LoRA to emphasize its advantages over conventional transfer learning approaches. Our study included a comparison on a smaller dataset featuring three distinct settings: ARViT trained from scratch (ARViT-Scratch), ARViT full fine-tuning using a pre-trained model (ARViT-TL), and ARViT enhanced with LoRA showing partial fine-tuning using a pre-trained model (ARViT-LoRA).

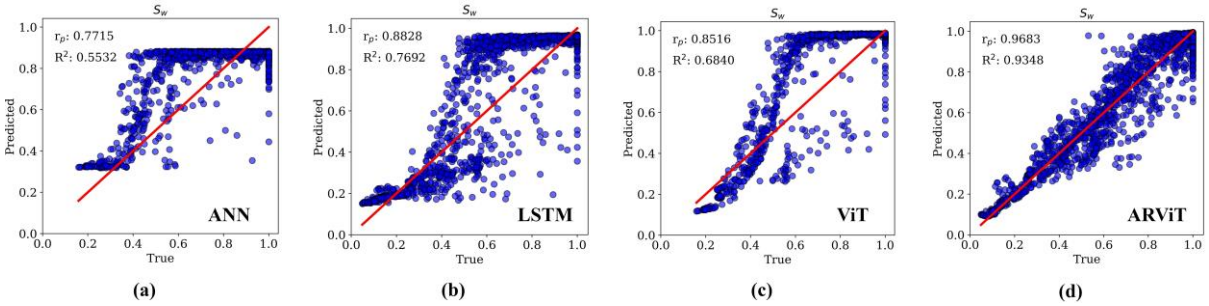

Figure 16 – Cross-Plots between True and Predicted Water Saturation from various models along with pearson coefficient and r2 score. (a) ANN, (b) LSTM, (c) ViT, and (d) ARViT. These cross-plots

offer insights into the performance and accuracy of each model in estimating water saturation, facilitating comparative analysis and model evaluation.

The results of this comparative analysis reveal insightful trends (Table 3). ARViT-Scratch, trained entirely from scratch, displayed the lowest model performance with an accuracy of 88.74% in lithology prediction and comparatively high MSE of 0.002 and 0.027 for ϕ and S_w prediction, respectively. In contrast, ARViT-TL, benefiting from transfer learning, exhibited a notable improvement, achieving 96.90% accuracy in lithology prediction, with MSE values of 0.0005 and 0.009 for ϕ and S_w prediction, respectively. However, the most remarkable performance enhancement was observed in ARViT-LoRA, where LoRA was applied during fine-tuning. This configuration yielded the highest accuracy, registering at 97.22% for lithology prediction. The MSE values for ϕ and S_w prediction in ARViT-LoRA were 0.0005 and 0.007, respectively.

Table 3. Performance Comparison of ARViT Models trained using smaller set (LoRA set) with different training Strategies and evaluation on blind set.

Model Name	**Lithology**		ϕ		S_w	
	Accuracy	**F1-Score**	**MSE**	**MAE**	**MSE**	**MAE**
ARViT-Scratch	88.74	71.16	0.0020	0.036	0.027	0.012
ARViT-TL	96.90	87.50	0.0005	0.017	0.009	0.058
ARViT-LoRA	**97.22**	87.33	**0.0005**	**0.017**	**0.007**	**0.053**

Beyond performance gains, the utilization of LoRA offered several additional benefits. Most notably, LoRA served as an effective safeguard against overfitting during transfer learning. Moreover, it significantly reduced the number of trainable parameters, attributed to it's partial fine-tuning approach, resulting in decreased memory consumption, thereby contributing to reduced carbon emissions. Specifically, the total number of trainable parameters in the

original ARViT model amounted to 769,711. Post-application of LoRA, this number decreased dramatically to a mere 15,933 trainable parameters, representing just 2.08% of the original parameter count. This reduction translated into a substantial decrease in GPU usage, with earlier GPU consumption measured at approximately 6,126 megabytes, while the new GPU consumption decreased to 4,678 megabytes, marking a noteworthy 25% reduction in GPU usage. These findings highlight LoRA's crucial role in not only improving model efficiency but also in promoting sustainability by minimizing resource utilization.

6. Conclusion

In this study, our primary goal was to devise a unified model using an auto-regressive self-attention based multitasking framework to jointly optimize multiple tasks along with the optimization of computational resources required while enhancing interpretability, prediction capabilities and adaptability to new dataset. We aim to develop a model capable of concurrently addressing various tasks, including lithology prediction, porosity estimation, and water saturation estimation, using self-attentive deep-learning models applied to well logs.

Through series of experimentation, ARViT emerged as the top-performing model, giving accuracy of 96.51% in lithology prediction and MSE of 0.0004 and 0.005 in estimating ϕ and S_w, respectively; surpassing alternate models such as ANN, LSTM, and ViT. Its sequential processing of output played a crucial role in achieving better performance that it's counterpart. By consolidating multiple tasks into a single model, we enhanced knowledge sharing between tasks. A single unified model now manages the three tasks that were previously handled by three separate models resulting in an approximately threefold reduction in GPU consumption when calculating these three petrophysical properties. Moreover, incorporating LoRA into the ARViT model further enhanced the adaptability of the ARViT with smaller unseen datasets, giving accuracy of 97.22% in lithology prediction

and MSE of 0.0005 and 0.007 in estimating ϕ and S_w, respectively; reducing overfitting risks. LoRA also reduced the number of trainable parameters within ARViT which further led to additional 25% decrease in GPU usage and computational cost, lowering carbon emissions and adhering to sustainable computing practices. This approach marks the first application of LoRA in geoscience and represents a crucial step forward in efficiently adapting knowledge from one field or basin to another.

While our study highlights various advantages such as unified model, reduced computational costs, improved model performances and adaptibility, and streamlined interpretation processes, there is still room for improvement in enhancing water saturation performance, which could be addressed in future studies. In future research, integrating additional logs such as SP and incorporating additional feature-engineered logs could enhance S_w prediction. Alternatively, researchers may explore the implementation of parallel networks alongside the main network, incorporating constant well logging records such as mud information (type, resistivity, and temperature) to improve model accuracy. The impact of artifacts of the well logs on the performance of ViT and ARViT could also be explored in future. Our approach significantly differs from previous research by consolidating knowledge from multiple tasks into one model with the help of self-attention, auto-regression, joint-optimization and multitasking for greater accuracy and efficiency. Additionally, our utilization of partial fine-tuning-based LoRA presents a novel and more computationally efficient alternative to traditional full fine-tuning-based transfer learning approaches used in prior methodologies. Overall our proposed approach of ARViT and LoRA contributes to the advancement of deep learning applications in geoscience, offering a more efficient approach to petrophysical properties estimation.

7. Acknowledgement

We would like to express our sincere gratitude to the anonymous reviewers for their valuable feedback and constructive criticism, which significantly contributed to enhancing the comprehensiveness and readability of this work. Special thanks to Laraib Abbas for their thorough review and insightful comments on the manuscript. We also extend our gratitude to the Alberta Energy Regulator for open-sourcing the data, which was invaluable for conducting this research. We acknowledge the use of the Generic Mapping Tool (GMT) software (Wessel et al., 2013), in visualizing our study area, and extend our appreciation to Shirish Bose for their assistance in creating the same. We also acknowledge the use of Generative AI tools for paraphrasing the sentences for enhanced readability and confirm that all the information provided is cross verifired by the authors.

8. References

Ahmadi, M.A., Chen, Z., 2019. Comparison of machine learning methods for estimating permeability and porosity of oil reservoirs via petro-physical logs. Petroleum 5. https://doi.org/10.1016/j.petlm.2018.06.002

Alaudah, Y., Michałowicz, P., Alfarraj, M., Alregib, G., 2019. A machine-learning benchmark for facies classification. Interpretation 7. https://doi.org/10.1190/INT-2018-0249.1

Alzubaidi, F., Mostaghimi, P., Swietojanski, P., Clark, S.R., Armstrong, R.T., 2021. Automated lithology classification from drill core images using convolutional neural networks. J Pet Sci Eng 197. https://doi.org/10.1016/j.petrol.2020.107933

Anggara, D., Suarna, N., Arie Wijaya, Y., 2023. Performance Comparison Analysis Of Optimizer Adam, SGD, and RMSPROP on The H5 Model. Jurnal Ilmiah NERO 8.

Ba, J.L., Kiros, J.R., Hinton, G.E., 2015. (LN) Layer Norm. arXiv:1607.06450v1.

Burges, C.J.C., 1998. A tutorial on support vector machines for pattern recognition. Data Min Knowl Discov 2. https://doi.org/10.1023/A:1009715923555

Cho, K., Van Merriënboer, B., Gulcehre, C., Bahdanau, D., Bougares, F., Schwenk, H., Bengio, Y., 2014. Learning phrase representations using RNN encoder-decoder for statistical machine translation, in: EMNLP 2014 - 2014 Conference on Empirical Methods in Natural Language Processing, Proceedings of the Conference. https://doi.org/10.3115/v1/d14-1179

Cunningham, P., Delany, S.J., 2021. K-Nearest Neighbour Classifiers-A Tutorial. ACM Comput Surv. https://doi.org/10.1145/3459665

Dosovitskiy, A., Beyer, L., Kolesnikov, A., Weissenborn, D., Zhai, X., Unterthiner, T., Dehghani, M., Minderer, M., Heigold, G., Gelly, S., Uszkoreit, J., Houlsby, N., 2021. AN IMAGE IS WORTH 16X16 WORDS: TRANSFORMERS FOR IMAGE RECOGNITION AT SCALE, in: ICLR 2021 - 9th International Conference on Learning Representations.

Duchi, J., Hazan, E., Singer, Y., 2011. Adaptive subgradient methods for online learning and stochastic optimization. Journal of Machine Learning Research 12.

Elshamy, R., Abu-Elnasr, O., Elhoseny, M., Elmougy, S., 2023. Improving the efficiency of RMSProp optimizer by utilizing Nestrove in deep learning. Sci Rep 13. https://doi.org/10.1038/s41598-023-35663-x

Flach, P.D., 1984. Oil sands geology - Athabasca deposits north. Geological Survey Department, Alberta Research Council Edmonton, Alberta, Canada.

Glorot, X., Bengio, Y., 2010. Understanding the difficulty of training deep feedforward neural networks, in: Journal of Machine Learning Research.

Hadavimoghaddam, F., Ostadhassan, M., Sadri, M.A., Bondarenko, T., Chebyshev, I., Semnani, A., 2021. Prediction of water saturation from well log data by machine learning algorithms: Boosting and super learner. J Mar Sci Eng 9. https://doi.org/10.3390/jmse9060666

He, K., Zhang, X., Ren, S., Sun, J., 2016. Deep residual learning for image recognition, in: Proceedings of the IEEE Computer Society Conference on Computer Vision and Pattern Recognition. https://doi.org/10.1109/CVPR.2016.90

Hein, F.J., Cotterill, D.K., Berhane, H., 2000. An atlas of lithofacies of the McMurray Formation Athabasca Oil Sands deposit, northeastern Alberta; surface and subsurface. Earth Sciences Report 2000-07.

Hu, E., Shen, Y., Wallis, P., Allen-Zhu, Z., Li, Y., Wang, S., Wang, L., Chen, W., 2022. LORA: LOW-RANK ADAPTATION OF LARGE LANGUAGE MODELS, in: ICLR 2022 - 10th International Conference on Learning Representations.

Ibrahim, A.F., Elkatatny, S., Al Ramadan, M., 2022. Prediction of Water Saturation in Tight Gas Sandstone Formation Using Artificial Intelligence. ACS Omega 7. https://doi.org/10.1021/acsomega.1c04416

Jang, J.S.R., 1993. ANFIS: Adaptive-Network-Based Fuzzy Inference System. IEEE Trans Syst Man Cybern 23. https://doi.org/10.1109/21.256541

Jiang, C., Zhang, D., Chen, S., 2021. Lithology identification from well log curves via neural networks with additional geological constraint. Geophysics 86. https://doi.org/10.1190/geo2020-0676.1

Ke, G., He, D., Liu, T.Y., 2021. RETHINKING POSITIONAL ENCODING IN LANGUAGE PRE-TRAINING, in: ICLR 2021 - 9th International Conference on Learning Representations.

Khalifa, H., Tomomewo, O.S., Ndulue, U.F., Berrehal, B.E., 2023. Machine Learning-Based Real-Time Prediction of Formation Lithology and Tops Using Drilling Parameters with a Web App Integration. Eng 4. https://doi.org/10.3390/eng4030139

Kingma, D.P., Ba, J.L., 2015. Adam: A method for stochastic optimization, in: 3rd International Conference on Learning Representations, ICLR 2015 - Conference Track Proceedings.

Kumar, A., 2021. Transformer-Based Deep Learning Models for Well Log Processing and Quality Control by Modelling Global Dependence of the Complex Sequences, in: Society of Petroleum Engineers - Abu Dhabi International Petroleum Exhibition and Conference, ADIP 2021. https://doi.org/10.2118/208109-MS

Kumar, T., Seelam, N.K., Rao, G.S., 2022. Lithology prediction from well log data using machine learning techniques: A case study from Talcher coalfield, Eastern India. J Appl Geophy 199. https://doi.org/10.1016/j.jappgeo.2022.104605

Lin, Z., Feng, M., Dos Santos, C.N., Yu, M., Xiang, B., Zhou, B., Bengio, Y., 2017. A structured self-attentive sentence embedding, in: 5th International Conference on Learning Representations, ICLR 2017 - Conference Track Proceedings.

Meshalkin, Y., Shakirov, A., Orlov, D., Koroteev, D., 2020. Well-logging based lithology prediction using machine learning, in: Data Science in Oil and Gas 2020. https://doi.org/10.3997/2214-4609.202054010

Miah, M.I., Zendehboudi, S., Ahmed, S., 2020. Log data-driven model and feature ranking for water saturation prediction using machine learning approach. J Pet Sci Eng 194. https://doi.org/10.1016/j.petrol.2020.107291

Mishra, A., Sharma, A., Patidar, A.K., 2022. Evaluation and Development of a Predictive Model for Geophysical Well Log Data Analysis and Reservoir Characterization: Machine Learning Applications to Lithology Prediction. Natural Resources Research 31. https://doi.org/10.1007/s11053-022-10121-z

Mohamed, I.M., Mohamed, S., Mazher, I., Chester, P., 2019. Formation lithology classification: Insights into machine learning methods, in: Proceedings - SPE Annual Technical Conference and Exhibition. https://doi.org/10.2118/196096-ms

Mossop, G.D., 1980. Geology of the Athabasca oil sands. Science (1979) 207. https://doi.org/10.1126/science.207.4427.145

Mustafa, A., Tariq, Z., Mahmoud, M., Abdulraheem, A., 2023. Machine learning accelerated approach to infer nuclear magnetic resonance porosity for a middle eastern carbonate reservoir. Sci Rep 13. https://doi.org/10.1038/s41598-023-30708-7

Nasim, M.Q., Maiti, T., Srivastava, A., Singh, T., Mei, J., 2022. Seismic Facies Analysis: A Deep Domain Adaptation Approach. IEEE Transactions on Geoscience and Remote Sensing 60. https://doi.org/10.1109/TGRS.2022.3151883

Nasim, M.Q., Patwardhan, N., Ali, J., Maiti, T., Marrone, S., Singh, T., Sansone, C., 2024a. Digitizer: A Synthetic Dataset for Well-Log Analysis, in: Lecture Notes in Computer Science (Including Subseries Lecture Notes in Artificial Intelligence and Lecture Notes in Bioinformatics). https://doi.org/10.1007/978-3-031-51023-6_9

Nasim, M.Q., Patwardhan, N., Maiti, T., Marrone, S., Singh, T., 2023. VeerNet: Using Deep Neural Networks for Curve Classification and Digitization of Raster Well-Log Images. J Imaging 9. https://doi.org/10.3390/jimaging9070136

Nasim, M.Q., Roy, P.N.S., Mitra, A., 2024b. Joint Optimization of Lithology and Petrophysical Parameters in Athabasca Oil Sands Using Self-Attention Mechanism. General Assembly 2024, European Geosciences Union (EGU). https://doi.org/10.5194/egusphere-egu24-14109

Pedregosa, F., Varoquaux, G., Gramfort, A., Michel, V., Thirion, B., Grisel, O., Blondel, M., Prettenhofer, P., Weiss, R., Dubourg, V., Vanderplas, J., Passos, A., Cournapeau, D., Brucher, M., Perrot, M., Duchesnay, É., 2011. Scikit-learn: Machine learning in Python. Journal of Machine Learning Research 12.

Ranger, M.J., Pemberton, S.G., 1997. Elements of a stratigraphic framework for the McMurray Formation in south Athabasca area, Alberta, in: Petroleum Geology of the Cretaceous Mannville Group, Western Canada.

Sang, W., Yuan, S., Han, H., Liu, H., Yu, Y., 2023. Porosity prediction using semi-supervised learning with biased well log data for improving estimation accuracy and reducing prediction uncertainty. Geophys J Int 232. https://doi.org/10.1093/gji/ggac371

Serra, O., 1986. Fundamentals of well-log interpretation, 2. The interpretation of logging data. Fundamentals of well-log interpretation, 2. The interpretation of logging data.

Serra, O., 1964. The Fundamentals of Well Log Interpretation, Science.

Sinaga, K.P., Yang, M.S., 2020. Unsupervised K-means clustering algorithm. IEEE Access 8. https://doi.org/10.1109/ACCESS.2020.2988796

Sun, J., Chen, M., Li, Q., Ren, L., Dou, M., Zhang, J., 2021. A new method for predicting formation lithology while drilling at horizontal well bit. J Pet Sci Eng 196. https://doi.org/10.1016/j.petrol.2020.107955

Sun, Y., Pang, S., Zhang, J., Zhang, Y., 2024. Porosity prediction through well logging data: A combined approach of convolutional neural network and transformer model (CNN-transformer). Physics of Fluids 36. https://doi.org/10.1063/5.0190078

Vaswani, A., Shazeer, N., Parmar, N., Uszkoreit, J., Jones, L., Gomez, A.N., Kaiser, Ł., Polosukhin, I., 2017. Attention is all you need, in: Advances in Neural Information Processing Systems.

Wang, F., Yang, B., Wang, Y., Wang, M., 2022. Learning From Noisy Data: An Unsupervised Random Denoising Method for Seismic Data Using Model-Based Deep

Learning. IEEE Transactions on Geoscience and Remote Sensing 60. https://doi.org/10.1109/TGRS.2022.3165037

Wang, J., Cao, J., Fu, J., Xu, H., 2022. Missing well logs prediction using deep learning integrated neural network with the self-attention mechanism. Energy 261. https://doi.org/10.1016/j.energy.2022.125270

Wessel, P., Smith, W.H.F., Scharroo, R., Luis, J., Wobbe, F., 2013. Generic Mapping Tools: Improved Version Released. Eos, Transactions American Geophysical Union 94, 409–410. https://doi.org/10.1002/2013EO450001

Wightman, D.M., Attalla, M.N., Wynne, D.A., Strobl, R.S., Berhane, H., Cotterill, D.K. and Berezniuk, T., 1995. Resource characterization of the McMurray/Wabiskaw deposit in the Athabasca oil sands area: a synthesis, AOSTRA technical publication series.

Wold, S., Esbensen, K., Geladi, P., 1987. Principal component analysis. Chemometrics and Intelligent Laboratory Systems 2. https://doi.org/10.1016/0169-7439(87)80084-9

Wynne, D.A., Attalla, M., Berezniuk, T., Berhane, H., Brulotte, M., Cotterill, D.K., Strobl, R., Wightman, D.M., 1995. Athabasca Oil Sands data McMurray/Wabiskaw oil sands deposit - electronic data.

Xie, Y., Zhu, C., Zhou, W., Li, Z., Liu, X., Tu, M., 2018. Evaluation of machine learning methods for formation lithology identification: A comparison of tuning processes and model performances. J Pet Sci Eng 160. https://doi.org/10.1016/j.petrol.2017.10.028

Xiong, R., Yang, Y., He, D., Zheng, K., Zheng, S., Xing, C., Zhang, H., Lan, Y., Wang, L., Liu, T.Y., 2020. On layer normalization in the transformer architecture, in: 37th International Conference on Machine Learning, ICML 2020.

Yang, F., Ma, J., 2019. Deep-learning inversion: A next-generation seismic velocity model building method. Geophysics 84. https://doi.org/10.1190/geo2018-0249.1

Zhang, Q., Wei, C., Wang, Y., Du, S., Zhou, Y., Song, H., 2019. Potential for prediction of water saturation distribution in reservoirs utilizing machine learning methods. Energies (Basel) 12. https://doi.org/10.3390/en12193597

Zhang, Z., Wang, Y., Wang, P., 2021. On a deep learning method of estimating reservoir porosity. Math Probl Eng 2021. https://doi.org/10.1155/2021/6641678

Zhekenov, T., Nechaev, A., Chettykbayeva, K., Zinovyev, A., Sardarov, G., Tatur, O., Petrakov, Y., Sobolev, A., 2021. Application of machine learning for lithology-on-bit prediction using drilling data in real-time, in: Society of Petroleum Engineers - SPE Russian Petroleum Technology Conference 2021, RPTC 2021. https://doi.org/10.2118/SPE-206622-MS

Zhou, G., Zhou, Y., Huang, H., Tang, Z., 2019. Functional networks and applications: A survey. Neurocomputing 335. https://doi.org/10.1016/j.neucom.2018.04.085